ACS APPLIED MATERIALS & INTERFACES

Research Article

www.acsami.org

Donor–Acceptor Small Molecules for Organic Photovoltaics: Single-Atom Substitution (Se or S)

Xiaoming He,[†,‡,§] Bing Cao,[†,‡,§] Tate C. Hauger,[†,‡] Minkyu Kang,[†,‡] Sergey Gusarov,[†] Erik J. Luber,[†,‡] and Jillian M. Buriak*[,†,‡]

[†]National Institute for Nanotechnology, National Research Council, 11421 Saskatchewan Drive, Edmonton, Alberta T6G 2M9, Canada

[‡]Department of Chemistry, University of Alberta, Edmonton, Alberta T6G 2G2, Canada

Supporting Information

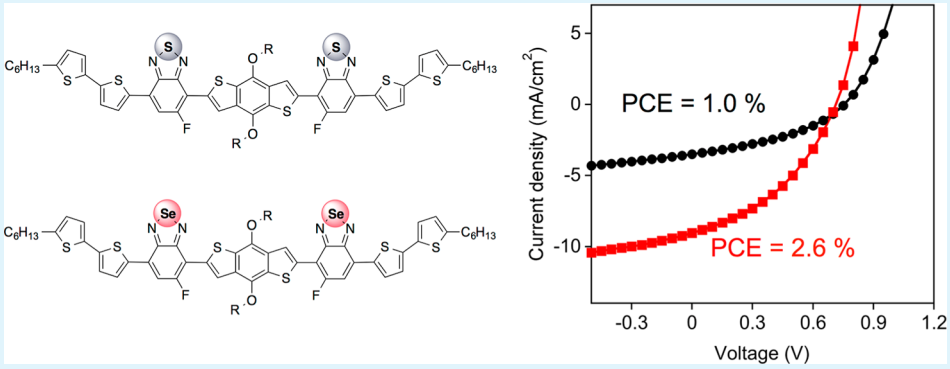

ABSTRACT: Two isostructural low-band-gap small molecules that contain a one-atom substitution, S for Se, were designed and synthesized. The molecule 7,7′-[4,8-bis(2-ethylhexyloxy)benzo[1,2-*b*:4,5-*b*′]dithiophene]bis[6-fluoro-4-(5′-hexyl-2,2′-bithiophen-5-yl)benzo[*c*][1,2,5]thiadiazole] (**1**) and its selenium analogue 7,7′-[4,8-bis(2-ethylhexyloxy)benzo[1,2-*b*:4,5-*b*′]-dithiophene]bis[6-fluoro-4-(5′-hexyl-2,2′-bithiophen-5-yl)benzo[*c*][1,2,5]selenodiazole] (**2**) are both based on the electron-rich central unit benzo[1,2-*b*:4,5-*b*′]dithiophene. The aim of this work was to investigate the effect of one-atom substitution on the optoelectronic properties and photovoltaic performance of devices. Theoretical calculations revealed that this one-atom variation has a small but measurable effect on the energy of frontier molecular orbital (HOMO and LUMO), which, in turn, can affect the absorption profile of the molecules, both neat and when mixed in a bulk heterojunction (BHJ) with $PC_{71}BM$. The Se-containing variant **2** led to higher efficiencies [highest power conversion efficiency (PCE) of 2.6%] in a standard organic photovoltaic architecture, when combined with $PC_{71}BM$ after a brief thermal annealing, than the S-containing molecule **1** (highest PCE of 1.0%). Studies of the resulting morphologies of BHJs based on **1** and **2** showed that one-atom substitution could engender important differences in the solubilities, which then influenced the crystal orientations of the small molecules within this thin layer. Brief thermal annealing resulted in rotation of the crystalline grains of both molecules to more energetically favorable configurations.

KEYWORDS: *organic photovoltaics, organic solar cell, bulk heterojunction, small molecules, selenium, sulfur*

INTRODUCTION

The development of clean and renewable energy alternatives to fossil-fuel-based sources has become one of the most important missions undertaken by modern science. Organic photovoltaics (OPVs) are a promising candidate for directly converting the energy in sunlight to electricity because of the potential economy of scale with regards to mass manufacturing.[1−3] Polymer-based OPVs that have a bulk heterojunction (BHJ) as their key design element have been studied extensively, particularly during the past decade.[4−7] These BHJ-based OPV devices typically contain a blend film of a p-type (electron-donating) conjugated polymer and an n-type (electron-accepting) fullerene derivative that, when mixed together, undergo nanoscale phase segregation.[8] The combination of regioregular poly(3-hexylthiophene) (P3HT) and [6,6]phenyl-C61-butyric acid methyl ester ($PC_{61}BM$), or [6,6]phenyl-C71-butyric acid methyl ester ($PC_{71}BM$), has become an OPV benchmark, with average power conversion efficiencies (PCEs) of around 3.5−4%.[4,9] This range of PCE values for this now standard combination represents the ceiling for this class of materials, mainly due to the limited absorption profile of the polythiophene-based P3HT polymer.[9]

In order to improve the PCE of OPV devices, there has been a great deal of exciting progress directed toward the synthesis of

Received: February 3, 2015
Accepted: March 26, 2015
Published: March 26, 2015

DOI: 10.1021/acsami.5b01063
ACS Appl. Mater. Interfaces 2015, 7, 8188−8199

Scheme 1. (a) Molecular Structures of *p*-DTS(FBTTh$_2$)$_2$, 1, and 2 and (b) Synthetic Routes toward 1 and 2

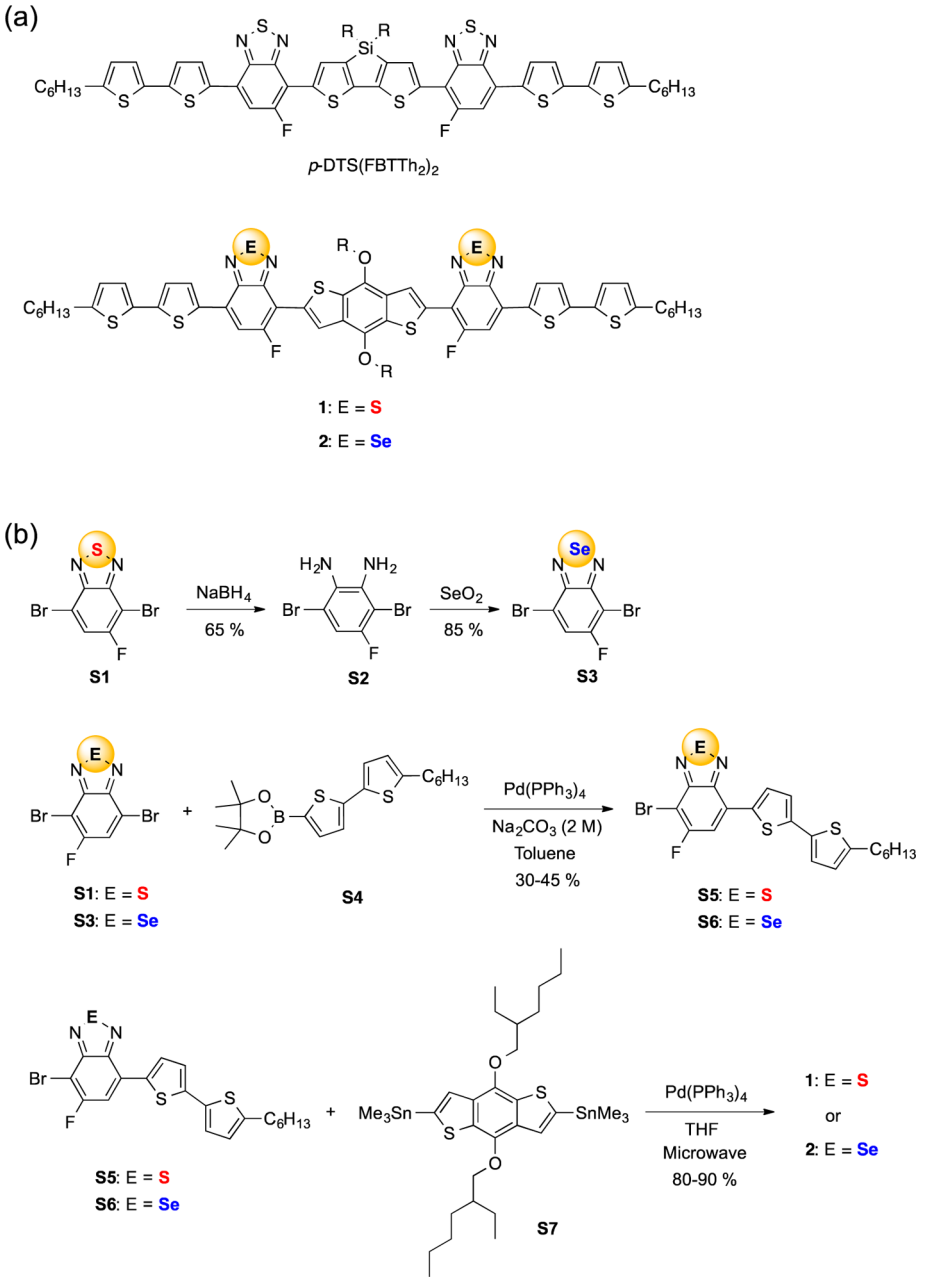

novel low-band-gap polymers that are based on an alternating donor–acceptor (D–A) design that improves light-harvesting properties through a better match with the sun's emission spectrum; reported PCEs are now reaching a very respectable 10%.[10−13] Despite the great success of these new conjugated polymers for OPV applications, they also suffer from intrinsic drawbacks, such as batch-to-batch variations that can hamper reproducibility.[14] Subtle differences in the molecular weight, polydispersity, and crystallinity of the final product can influence the solubility, mixing, and nanoscale phase segregation and can have a profound influence on the final morphology of the BHJ, and hence on the resulting device performance.[15]

Conjugated small molecules represent an intriguing alternative to the widely studied polymer-based donors in OPVs due to their well-defined and uniform nature because, in a pure form, they are entirely monodisperse (polydispersity index of 1.0).[16−33] A number of examples of PCEs as high as 8–9% have been reported, comparable to those of low-band-gap polymers, but there are far fewer examples.[18−30] The shorter conjugated backbone, when compared with a polymer, renders the design of a low-band-gap material difficult. In addition, the generation of a nanoscale phase-segregated BHJ with a small-molecule donor and a (small-molecule) fullerene acceptor, which should contain nanocrystalline domains of both materials, is problematic because of the mutual miscibility of these two compounds; morphological control is therefore difficult. To tackle the challenge of designing a small molecule with a suitable band gap, the electronic characteristics can be manipulated via control of the intramolecular D–A combination. From a synthetic standpoint, small molecules are typically more easily synthesized than polymers, and one can therefore incorporate a range of different donor and acceptor units in a specific sequence, thus providing a precise approach to fine-tuning the

DOI: 10.1021/acsami.5b01063
ACS Appl. Mater. Interfaces 2015, 7, 8188–8199

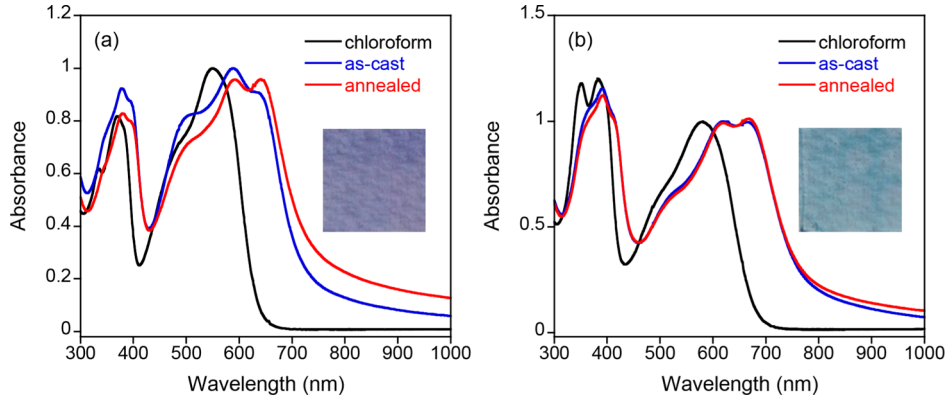

Figure 1. Normalized UV−vis absorption of (a) **1** and (b) **2** under different conditions. The black trace refers to a solution in $CHCl_3$ (1×10^{-5} M), the blue trace to a film spin-coated from a CB solution (**1** was spin-coated at 80 °C, and **2** was spin-coated at room temperature), and the red trace to the spin-coated film after annealing for 2 min at 80 °C in N_2. Insets show the colors of thin films of **1** and **2** on glass.

optoelectronic properties. Recently, Bazan and co-workers reported a class of small molecules with multiple alternating D−A (D1−A−D2−A−D1) chromophores;[27−30] one representative example is *p*-DTS(FBTTh$_2$)$_2$ (shown in Scheme 1a), which when coupled with $PC_{71}BM$, achieved a high PCE of 8.9%.[27,28] Further studies by the same group led to the development of new small-molecule donor materials through replacement of the central donor constituent with a silaindacenodithiophene unit, which resulted in PCEs of 4−6%, when paired with $PC_{71}BM$.[29] Another related study, by Chabinyc and co-workers, showed that a very subtle change of a single bridging atom, from Si to C, in the central donor unit led to a significant loss of PCE (less than 1%).[30] These results demonstrate that the multiple D1−A−D2−A−D1 chromophore configuration is a versatile framework and that systematic tuning of the different donor and/or acceptor fragments and configurations can have a dramatic effect on the resulting OPV performance. In addition, the identity of the central donor unit (D2) has been shown to be of great importance with respect to the optoelectronic properties as well as the device performance[27−30] but has been explored only cursorily; the relationship between the electron acceptor (A) unit and the photovoltaic performance remains ill-defined but is worth surveying further.

The S-containing benzothiadiazole (BT) unit is a well-known electron-acceptor unit that has been widely used in polymer-based high-efficiency OPVs.[34−37] Substitution of the S atom with heavier chalcogenides (e.g., Se, Te) in π-conjugated materials has created a promising route forward for expanding the repertoire of conjugated subunits because of their very unique structural (i.e., bonding) and electronic properties.[38−46] Replacement of thiophene with selenophene in a polymer backbone generally results in a lowering of the polymer band gap, and some of these selenophene-containing polymers exhibit higher photovoltaic efficiency.[38−46] Following the same trend with respect to the Se analogue of BT (benzoselenadiazole, BS), several research groups have shown that BS-containing polymers exhibit a red-shifted absorption spectrum relative to their BT-containing counterparts when combined with the same electron-donating moiety.[47−51] Another example of interesting research has revealed that benzoselenodiazole-containing small molecules assemble to form head-to-head dimers in the solid state because of a tendency to form intermolecular Se−N interactions.[52] Therefore, utilization of these two isostructural electron-acceptor units, BT and BS, in a small-molecule design is expected to affect the optical properties, molecular packing, and ultimately the photovoltaic performance.

Herein, we report two isostructural small molecules, 7,7′-[4,8-bis(2-ethylhexyloxy)benzo[1,2-*b*:4,5-*b*′]dithiophene]bis[6-fluoro-4-(5′-hexyl-2,2′-bithiophen-5-yl)benzo[*c*][1,2,5]-thiadiazole] (**1**) and its selenium analogue 7,7′-[4,8-bis(2-ethylhexyloxy)benzo[1,2-*b*:4,5-*b*′]dithiophene]bis[6-fluoro-4-(5′-hexyl-2,2′-bithiophen-5-yl)benzo[*c*][1,2,5]selenodiazole] (**2**), shown in Scheme 1a. The architecture of these two materials is based on a D1−A−D2−A−D1 chromophore configuration, with the electron-rich benzo[1,2-*b*:4,5-*b*′]-dithiophene (BDT) as the central donor unit (D2) and bithiophene end-capping donor units (D1). BDT was chosen as the central core because it is a well-known electron-donating unit and has been widely utilized as a key building block in low-band-gap polymers and small molecules for efficient solar cells.[53−55] The main aim of this work was to investigate the effect of one-atom substitution of S with Se in the acceptor unit (A) on the optoelectronic properties and photovoltaic performance of devices incorporating these small molecules.

RESULTS AND DISCUSSION

Synthesis and Physical Properties of 1 and 2. The synthetic routes for **1** and **2**, as well as several key intermediates, **S3**, **S5**, and **S6**, are summarized in Scheme 1b. 4,7-Dibromo-5-fluorobenzo[*c*][1,2,5]thiadiazole (**S1**) was prepared according to a reported procedure.[27] The Se analogue **S3** was synthesized from **S1** in high yield (56% overall yield in two steps). Reduction of **S1** using excess $NaBH_4$ led to the diamine intermediate **S2**, followed by reoxidation with SeO_2 to form the Se-containing molecule, **S3**. Subsequently, the asymmetric dibromo species (**S1** or **S3**) was then selectively reacted with 5′-hexyl-2,2′-bithiophene-5-boronic acid pinacol ester (**S4**) via Suzuki coupling to afford **S5** and **S6** in modest yield (30−45%). **S5** and **S6** were then coupled with the BDT donor unit **S7** through a Stille coupling to afford **1** and **2** in high yield (80−90%). These two final products were fully characterized by multinuclear NMR (^{1}H, ^{13}C, and ^{19}F) spectroscopy, high-resolution mass spectrometry (HRMS), and elemental analysis. The solubility of **1** (ca. 20 mg mL^{-1}) in chlorobenzene (CB) at room temperature is substantially lower than that of **2** (ca. 40 mg mL^{-1}). The difference in the solubility is contrary to the expectations of intermolecular Se−Se bonding in the solid state, which should decrease the solubility. In the case of these small molecules, however, π−π stacking and pendant alkyl chain

DOI: 10.1021/acsami.5b01063
ACS Appl. Mater. Interfaces 2015, 7, 8188−8199

Table 1. Optoelectronic Properties of 1 and 2

	λ_{abs} (ε^a) in $CHCl_3$		λ_{abs} in film				
compound	λ_{max}	λ_{onset}	λ_{max}	λ_{onset}	$E_{HOMO}{}^b$ (calcd) [eV]^c	E_{LUMO} (calcd) [eV]	$E_g{}^d$ (calcd) [eV]
1/**1′**	369 (4450), 550 (5440)	651	378, 589	735	−5.4 (−5.08)	−3.7 (−3.13)	1.7 (1.96)
2/**2′**	351 (6990), 382 (7120), 581 (5920)	694	390, 621, 665	784	−5.2 (−5.03)	−3.6 (−3.18)	1.6 (1.85)

^{a}Molar extinction coefficient ($dm^3\ mol^{-1}\ cm^{-1}$). ^{b}Measured by UPS. ^{c}DFT calculations based on the B3LYP/6-31+G(d,p) level of theory for **1′** and **2′**. ^{d}Determined from the onset of films as taken by UV−vis. E_{LUMO} was calculated as per $E_{LUMO} = E_{HOMO} + E_g$.

interactions dominate (vide infra); because Se has a larger atomic radius than S, the interplane distance for $\pi-\pi$ stacking would be expected to increase,[56] as has been seen earlier, thus leading to a weakening of the strength of this interaction in the solid state. The thermal stability was evaluated by thermogravimetric analysis (TGA), and the decomposition temperatures (T_d, defined as the temperature corresponding to >5% mass loss) for **1** and **2** were determined to be 335 and 310 °C, respectively, indicating high thermal stability (Figure S1 in the Supporting Information, SI). The melting temperatures (T_m) for **1** and **2**, determined by differential scanning calorimetry (DSC), are 243 and 237 °C, respectively.

Optoelectronic Properties. Figure 1 and Table 1 show the UV−vis absorption spectra of **1** and **2** in solution and as films on a glass substrate and the corresponding photophysical data (Table 2). In a $CHCl_3$ solution, **1** displays absorption

Table 2. Physical Properties of 1 and 2

compound	$T_m{}^a$ [°C]	$T_d{}^b$ [°C]	solubility^c [mg mL^{-1}]
1	243	335	20
2	237	310	40

^{a}Melting temperature (T_m) determined by DSC. ^{b}Decomposition temperature (T_d) determined by TGA. ^{c}In CB, at 21 °C.

maxima at λ_{max} = 369 (ε = 4450) and 550 nm (ε = 5440), while the absorption maxima of **2** are located at λ_{max} = 351 (ε = 6990), 382 (ε = 7120), and 581 nm (ε = 5920); the absorption profile of the Se-containing **2** is red-shifted ∼30 nm compared to that of **1** and has higher extinction coefficients. A similar red shift was also observed upon comparison of the two molecules in film form, with the films of **1** and **2** appearing purple and aqua, respectively (maxima: for **1**, λ_{max} = 378 and 589 nm; for **2**, λ_{max} = 390, 621, and 665 nm). Such red shifting of the absorption maxima upon moving from S to Se is most likely due to the lower ionization potential of the larger atom (Se), which, in turn, leads to a shallow highest occupied molecular orbital (HOMO) level and a smaller band gap.[57] Moreover, the absorption profiles of thin films of both compounds exhibit vibronic structuring in the 500−700 nm region, with a significant red shift compared to that of the solution, which is typical of a more ordered structure in the film state.[23,24,58] Upon brief thermal annealing (80 °C for 2 min, under N_2), the film absorbance of **1** undergoes a small red shift of approximately 5 nm, with a slightly enhanced peak intensity ratio of A_{640}/A_{585}, suggestive of increased molecular order.[29,59,60] No obvious red shift, akin to that seen upon annealing films of **1**, was observed for **2**, perhaps because of prior aggregation at room temperature before annealing, as suggested by X-ray diffraction (XRD; vide infra).

From the onset of film absorption (for **1**, λ_{onset} = 735 nm; for **2**, λ_{onset} = 784 nm), the optical band gaps of **1** and **2** were estimated to be 1.7 and 1.6 eV, respectively. A smaller band gap for Se-containing compounds, when compared to their S-containing congeners, has been observed in many other conjugated systems.[35−45,47−51,57] Ultraviolet photoelectron spectroscopy (UPS) was employed to determine the HOMO levels of **1** and **2** (Figure S2 and Table S1 in the SI), and they were calculated to be −5.4 and −5.2 eV, respectively. The deeper HOMO level of **1** is consistent with the higher ionization potential of S than Se.[56,57]

Theoretical Analysis. To better understand the optical and electronic characteristics of these two molecules, density functional theory (DFT) calculations [B3LYP/6-31+G(d,p) level of theory][61] were performed on **1** and **2**. For simplicity, the ethylhexyl and hexyl groups were replaced by methyl substituents; these compounds were labeled **1′** and **2′**. Both compounds adopt a highly planar structure in the optimized structure, suggesting extended π conjugation along the length of the molecule. The HOMO and lowest unoccupied molecular orbital (LUMO) energy isosurfaces and energy levels are shown in Figure 2 and Table 1 and appear quite similar for **1′** and **2′**. The HOMOs of both small molecules are extensively delocalized, while the LUMOs are located mainly on the electron-accepting BT (for **1′**) or BS (for **2′**) units. Interestingly, with respect to the BT and BS units, the

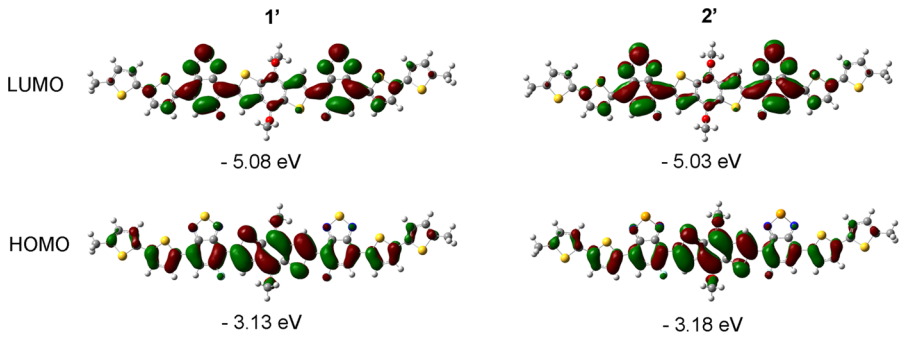

Figure 2. Frontier molecular orbital isosurfaces and energy levels using DFT calculations based on the B3LYP/6-31+G(d,p) level of theory for **1′** and **2′**.

DOI: 10.1021/acsami.5b01063
ACS Appl. Mater. Interfaces 2015, 7, 8188−8199

Table 3. Photovoltaic Characteristics of BHJ Solar Cells with Active Layers of 1 or 2 and $PC_{71}BM$ at Different Ratios

compound	blend ratio[a]	thermal annealing[b]	J_{sc} [mA cm^{-2}]	V_{oc} [V]	FF	average PCE [%]
1[c]	1.5:1	N	3.6 ± 0.2	0.64 ± 0.01	0.46 ± 0.10	1.0 ± 0.1
	1.5:1	Y	3.6 ± 0.1	0.66 ± 0.10	0.46 ± 0.01	1.0 ± 0.1
2[c]	1.5:1	N	7.2 ± 0.1	0.66 ± 0.10	0.35 ± 0.10	1.7 ± 0.1
	1.5:1	Y	7.0 ± 0.2	0.68 ± 0.10	0.35 ± 0.10	1.7 ± 0.1
2[d]	1.5:1	N	5.3 ± 0.3	0.62 ± 0.05	0.33 ± 0.01	1.0 ± 0.1
	1:1	Y	6.5 ± 0.5	0.71 ± 0.10	0.40 ± 0.01	1.8 ± 0.2
	1.5:1	Y	8.9 ± 0.2	0.71 ± 0.10	0.40 ± 0.01	2.6 ± 0.1
	2:1	Y	8.2 ± 0.5	0.72 ± 0.01	0.44 ± 0.03	2.5 ± 0.1

[a]30 mg/mL in CB, spin-coated at 1500 rpm for 1 min. [b]Active layer thermally annealed at 80 °C for 2 min. [c]Spin-coated at 80 °C. [d]Spin-coated at room temperature.

HOMO has no contribution from the heteroatoms (S or Se), while the LUMO is affected significantly by the presence of these heteroatoms. The calculated HOMO and LUMO energies of **1′** are E_{HOMO} = −5.08 eV and E_{LUMO} = −3.13 eV, with a calculated energy gap of ΔE = 1.95 eV. **2′** has a higher HOMO level (E_{HOMO} = −5.03 eV), a lower LUMO level (E_{LUMO} = −3.18 eV), and a smaller band gap (ΔE = 1.85 eV), as summarized in Table 1. These trends are consistent with the experimental data derived from UV−vis and UPS spectroscopy for **1** and **2**.

Device Performance. Thin-film BHJ solar cells were fabricated with the architecture ITO/PEDOT:PSS/[**1** or **2**]:$PC_{71}BM$/LiF/Al/Mg and tested under one sun illumination (AM 1.5G, 100 mW cm^{-2}). Mg was chosen so that substrate temperatures do not exceed 60 °C during deposition and confound the studies on the annealing temperature, thanks to the low sublimation temperature of this element. The active layer was spin-coated from a CB solution at 80 °C (this elevated temperature is required because of the poor solubility of **1** at room temperature). All solution processing was carried out in air. As a starting point, the reported optimal conditions for devices based on the small-molecule *p*-DTS(FBTTh$_2$)$_2$ (Scheme 1a),[27] where the *p*-DTS(FBTTh$_2$)$_2$/$PC_{71}BM$ ratio was 1.5:1 (w/w), were used. Table 3 summarizes the device performance. First, when the devices were compared based on [**1** or **2**]/$PC_{71}BM$ prepared from solutions heated to 80 °C, the PCEs were 1.0 ± 0.1% and 1.7 ± 0.1%, respectively, with the most obvious difference observed with J_{sc}; the J_{sc} value of **2**/$PC_{71}BM$ was twice as high as that of **1**/$PC_{71}BM$. In both cases, subsequent thermal annealing had no effect on the PCE, and the parameters (J_{sc}, V_{oc}, and FF) were largely unchanged. However, when devices based on **2**/$PC_{71}BM$ were prepared at room temperature (PCE = 1.0 ± 0.1%) and then thermally annealed, the PCE improved significantly, to 2.6 ± 0.1%, with increases in J_{sc} (to 8.9 ± 0.2 mA cm^{-2}), V_{oc} (to 0.71 ± 0.10 V), and FF (to 0.40 ± 0.01). It is noted that devices of **1**/$PC_{71}BM$ could not be prepared at room temperature because of the low solubility of **1** at room temperature. Figure 3 shows the current density−voltage (*J*−*V*) curves of devices based on the BHJs of **1**/$PC_{71}BM$ (prepared at 80 °C) and **2**/$PC_{71}BM$ (prepared at 80 °C and room temperature), without and with thermal annealing, under 1 sun illumination (AM 1.5G, 100 mW cm^{-2}).

Because of the promising increase in the PCE observed with the BHJ based on **2**/$PC_{71}BM$, further optimization was carried out on this combination, with the results summarized in Tables 3 and 4. Variation of the thermal annealing times under nitrogen (1, 2, and 5 min) and temperatures (80, 100, and 120 °C) was also investigated (Tables S3 and S4 in the SI). A total of 2 min of thermal annealing was found to be marginally better than 1 min, but with 5 min of annealing, V_{oc} was lowered, leading to a drop of the PCE to below 2%, and thus all thermal annealing was carried out for 2 min. Increasing the **2**/$PC_{71}BM$

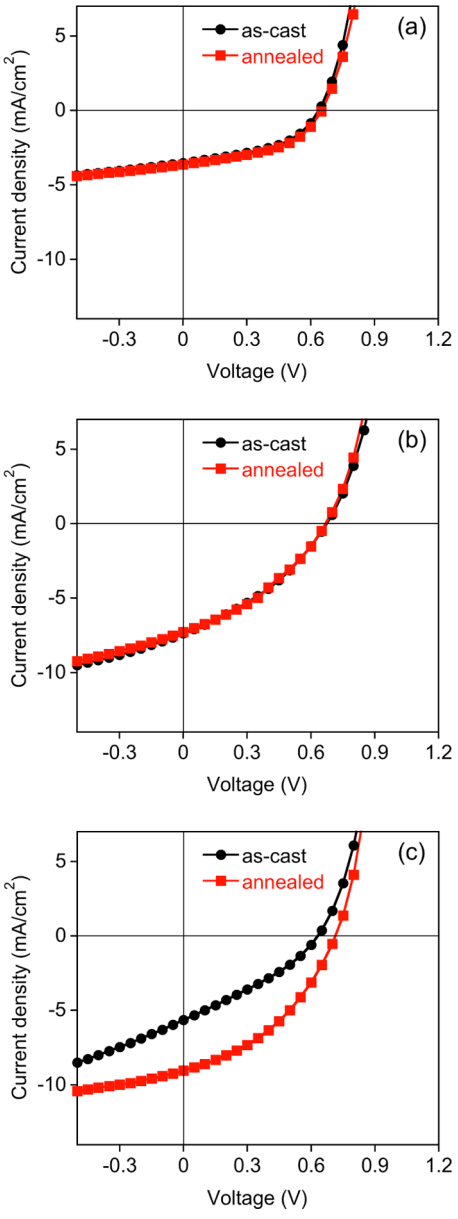

Figure 3. Typical *J*−*V* curves of (a) **1**/$PC_{71}BM$ spin-coated at 80 °C; (b) **2**/$PC_{71}BM$ spin-coated 80 °C; (c) **2**/$PC_{71}BM$ spin-coated at room temperature. The ratio of [**1** or **2**]/$PC_{71}BM$ was 1.5:1 (w/w).

DOI: 10.1021/acsami.5b01063
ACS Appl. Mater. Interfaces 2015, 7, 8188−8199

Table 4. Effect of the Film Thickness on the Device Performance Using 2/$PC_{71}BM$ (Ratio = 1.5:1, 30 mg/mL, Spin-Coated at Room Temperature)

spin rate [rpm]	acceleration rate [rpm s^{-1}]	film thickness [nm]	PCE [%]
600	900	181 ± 10	0.8 ± 0.1
1000	900	153 ± 5	1.1 ± 0.1
1200	900	133 ± 7	1.8 ± 0.2
1500	900	109 ± 3	2.6 ± 0.1
2000	900	89 ± 5	1.7 ± 0.2

ratio from 1.5:1 to 2:1 gave a similar PCE of 2.5 ± 0.1%, while a lower ratio of **2**/$PC_{71}BM$ of 1:1 resulted in a lower PCE of 1.8 ± 0.2%. The lowering of the PCE, with a higher loading of $PC_{71}BM$, could be ascribed to the inherent tendency of fullerene to aggregate under elevated temperatures, forming larger aggregates.[62,63] The effects of the addition of 1,8-diiodooctane (DIO), a commonly used high-boiling-point solvent additive that has improved the device performance in OPV devices, were examined, and unlike the system of *p*-DTS(FBTTh$_2$)$_2$:$PC_{71}BM$, reported by Bazan and co-workers,[23,27,28] the addition of DIO (0.5, 1.0, and 1.5%) to **2**/$PC_{71}BM$ did not enhance the PCE (Table S5 in the SI). Another aspect that is critical to the OPV performance is the thickness of the BHJ, and Table 4 summarizes the relationship between the spin-coating conditions and the organic film thickness, as well as the device performance, using a **2**/$PC_{71}BM$ (1.5:1, 30 mg/mL) blend. When the acceleration rate constant was kept at 900 rpm s^{-1}, changing the spin rate from 600 to 2000 rpm led to different film thicknesses ranging from 181 ± 10 to 89 ± 5 nm. The optimized spin rate was determined to be 1500 rpm, which gave a ∼109-nm-thick film, resulting in the reported average PCE of 2.6 ± 0.1%.

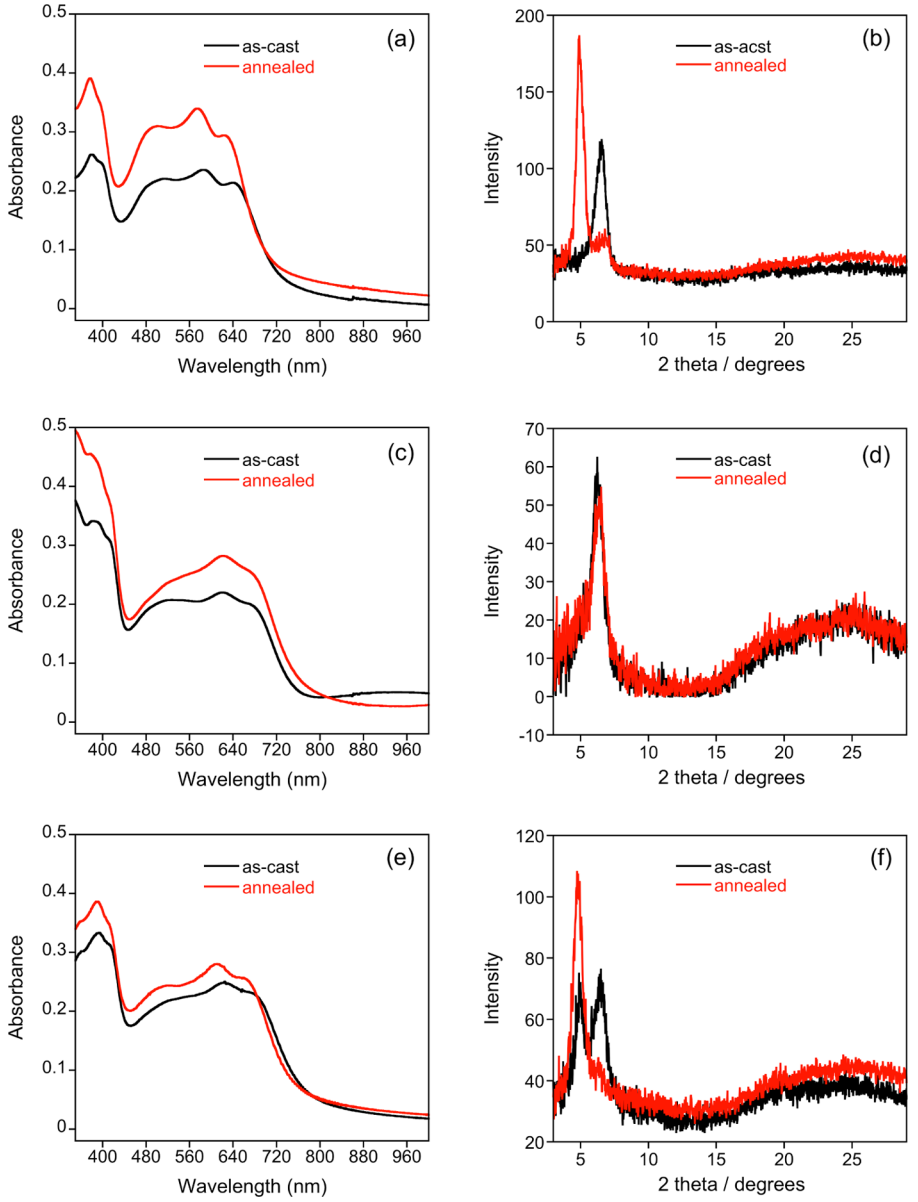

Figure 4. UV−vis and GIXRD spectra: (a and b) **1**/$PC_{71}BM$, spin-coated at 80 °C; (c and d) **2**/$PC_{71}BM$, spin-coated 80 °C; (e and f) **2**/$PC_{71}BM$ spin-coated at room temperature. The ratio of [**1** or **2**]/$PC_{71}BM$ is 1.5:1 (w/w). For the XRD samples, films were spin-coated on PEDOT:PSS/ITO substrates, and for the UV−vis spectra, films were spin-coated on glass.

DOI: 10.1021/acsami.5b01063
ACS Appl. Mater. Interfaces 2015, 7, 8188−8199

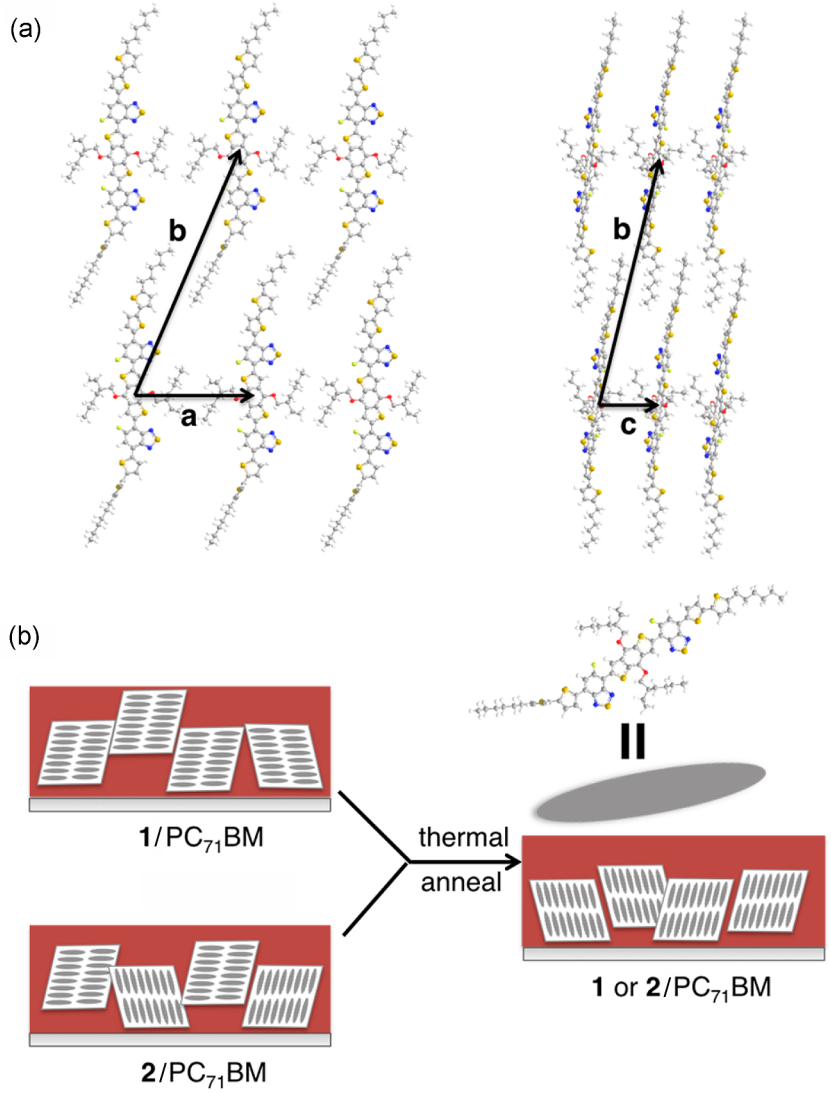

Figure 5. (a) Illustration showing the proposed crystal packing of the small molecules **1** and **2** in the BHJ. The unit cell is described by the lattice vectors **a**–**c**: **a**, ethylhexyl chain-packing direction, *d* spacing 13.0 Å; **b**, hexyl chain-packing direction; *d* spacing 18.4 Å; **c**, π–π stacking. (b) Proposed reorientation of the small-molecule crystal grains, in the BHJ, upon annealing.

Device Characterization. In order to gain insight into the effects of annealing and the difference in performances between devices fabricated from **1** and **2**, UV–vis, grazing-incidence X-ray diffraction (GIXRD), and atomic force microscopy (AFM) characterization of these devices was performed. Shown in Figure 4 are the UV–vis spectra of the as-cast devices (room temperature and 80 °C) and the annealed devices (annealing conditions: 80 °C, 2 min under nitrogen). In all cases, we see that there is a similar increase in absorbance in the visible spectrum. Similar increases of absorbance of small-molecule-based OPV devices upon thermal annealing have been attributed to better packing of the molecules in the film.[64] Given that all device configurations demonstrate similar as-cast UV–vis absorption profiles and increases in absorbance upon annealing, it is unlikely that these structural changes are responsible for the resulting differences in the device performance. Specifically, there does not appear to be any correlation between the changes in the device performance with an increase in UV–vis absorption. Devices cast at 80 °C have no change in their performance after annealing, while those cast at room temperature experience a significant increase in their performance, despite all devices having similar increases in UV–vis absorbance.

Also shown in Figure 4 are the corresponding GIXRD spectra of all device configurations before and after annealing at 80 °C. Upon inspection of the GIXRD spectra of **1**/$PC_{71}BM$ and **2**/$PC_{71}BM$ cast at 80 °C, we see that a single reflection at $2\theta = 6.8°$ is present, corresponding to a *d* spacing of 13.0 Å. Interestingly, the GIXRD spectra of annealed devices of **1**/$PC_{71}BM$ cast at 80 °C show significant changes, while the GIXRD spectra of annealed devices of **2**/$PC_{71}BM$ cast at 80 °C remain essentially unchanged. Specifically, a new reflection at $2\theta = 4.8°$ appears in **1**/$PC_{71}BM$ (corresponding a *d* spacing of 18.4 Å). It is possible that these two different *d* spacings correspond to the primary reflections from crystalline polymorphs of the small molecule. In this case, we would expect the more energetically stable, more compact (smaller lattice parameter) crystal structure to remain after annealing. However, the opposite trend is observed, which strongly suggests that the different *d* spacings do not correspond to different crystal structures. A likely explanation for the observed change in the GIXRD spectra is related to the relative

DOI: 10.1021/acsami.5b01063
ACS Appl. Mater. Interfaces 2015, 7, 8188–8199

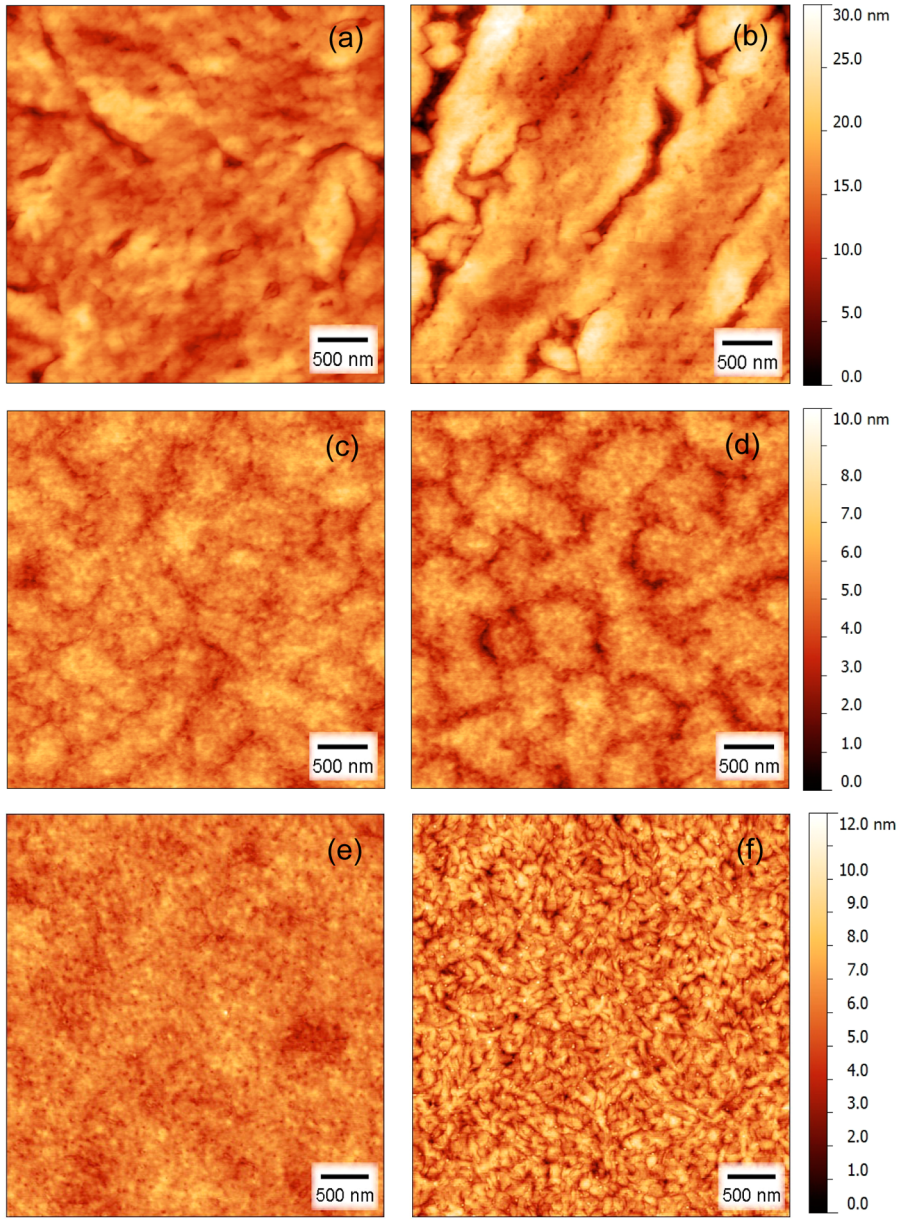

Figure 6. AFM topographic images: (a and b) **1**/$PC_{71}BM$, spin-coated at 80 °C; (c and d) **2**/$PC_{71}BM$, spin-coated 80 °C; (e and f) **2**/$PC_{71}BM$ spin-coated at room temperature. Images on the left (a, c, and e) correspond to the as-cast films and those on the right (b, d, and f) to the thermally annealed samples (80 °C for 2 min). Scan size: 4 × 4 μm^2. The ratio of [**1** or **2**]/$PC_{71}BM$ is 1.5:1 (w/w), and films were spin-coated on PEDOT:PSS/ITO substrates.

orientations of the crystalline grains, which rotate to more energetically favorable configurations upon annealing.[65,66] As such, the measured 13.0 and 18.4 Å *d* spacings likely correspond to two different in-plane lattice spacings. A proposed structure is shown in Figure 5a, where the 13.0 Å spacing corresponds to ethylhexyl chain packing and the 18.4 Å spacing to hexyl chain packing. We see that the molecular backbone packing distance of 18.4 Å is less than the length of the molecule along the alkyl side-chain direction, which is unsurprising given that an interdigitated configuration is expected to be energetically more stable because the small molecules would be efficiently packed.[67] Unfortunately, many attempts to grow single crystals of these two compounds for XRD failed. Fiber formation was observed in a 1:1 (v/v) $CHCl_3$/MeOH solvent combination for both compounds (Figure S3 in the SI); the widths were in the range of 100–400 nm.

The proposed reorientation of the small-molecule crystal grains upon annealing is depicted schematically in Figure 5b. In the case of **1**/$PC_{71}BM$, before annealing (as-cast), the conjugated backbone of **1** is parallel to the substrate and the incident X-rays, which explains why the feature corresponding to a *d* spacing of 18.4 Å is not observed by GIXRD (Figure 5b). Upon thermal annealing, almost all of the grains reorient such that the interdigitated planes of the crystallites of **1** are parallel to the substrate, with the molecular backbones close to perpendicular, and hence the feature at 18.4 Å dominates the GIXRD spectrum. A possible driving force for this observed reorientation of the crystal grains is a lower surface energy of the interdigitated orientation at the buried PEDOT:PSS/ITO interface.[68−70]

DOI: 10.1021/acsami.5b01063
ACS Appl. Mater. Interfaces 2015, 7, 8188−8199

For devices of **2**/$PC_{71}BM$ cast at room temperature, we see that the GIXRD spectra contain both reflections at 13.0 and 18.4 Å, which suggests that both grain orientations are present.[69] Similar to the **1**/$PC_{71}BM$ devices cast at 80 °C, after annealing most of the grains reorient such that the hexyl chains are packed parallel to the substrate.

It is noted that the GIXRD data are consistent with the UV−vis absorption data, where films that underwent crystal reorientation upon annealing (**1**/$PC_{71}BM$ spin-coated at 80 °C and **2**/$PC_{71}BM$ spin-coated at room temperature) show a small blue shift (Figure 4a,e), which could be due to H-aggregation.[60] Conversely, films that did not undergo crystal reorientation (**2**/$PC_{71}BM$ spin-coated from 80 °C) showed no shift in the UV−vis spectrum (Figure 4c). Much like the UV−vis data, we see that there is little correlation between the GIXRD spectra and the device performance; devices of **1**/$PC_{71}BM$ and **2**/$PC_{71}BM$ spin-coated at 80 °C have similar GIXRD spectra, but the **2**/$PC_{71}BM$ devices have nearly double the PCE. Following annealing, **1**/$PC_{71}BM$ exhibits a significant change in the grain reorientation, with no corresponding change in the device performance. Conversely, annealing of **2**/$PC_{71}BM$ cast at 80 °C displays no change in the GIXRD spectrum and no change in the device performance. Last, devices of **2**/$PC_{71}BM$ cast at room temperature have grains in both orientations, which reorient to the hexyl chain configuration after annealing, where a substantial increase in the PCE is observed.

From these UV−vis and GIXRD data, we see that the observed changes in the local structure (optical properties, crystallinity, and orientation) have little impact on the device performance. This suggests that the morphology of the BHJ (i.e., the spatial distribution of the small-molecule and $PC_{71}BM$ phases) plays an important role in the device performance. Shown in Figure 6 are the AFM micrographs of the as-cast devices (room temperature and 80 °C) and the annealed devices (80 °C). As-cast devices of **1**/$PC_{71}BM$ have a coarse surface morphology (micron-scale domains) with a root-mean-square (rms) roughness of 2.6 nm, with minimal further coarsening of the features upon thermal annealing at 80 °C for 2 min (rms roughness of 4.0 nm). As-cast devices of **2**/$PC_{71}BM$ at 80 °C appear to have a less coarse morphology than the **1**/$PC_{71}BM$ devices and also exhibit minimal coarsening with annealing. This more idealized distribution of phases within the BHJ morphology is a likely causative factor for the superior performance of the **2**/$PC_{71}BM$ devices cast at 80 °C. Last, we see that the devices of **2**/$PC_{71}BM$ cast at room temperature have a very fine morphology (rms roughness of 1.3 nm) but undergo significant coarsening of domain sizes after annealing, which are on the order of ∼10−20 nm. Given that these domain sizes are ideal for excition diffusion and dissociation in BHJs, this is likely the origin of the improved efficiency upon annealing of the room temperature cast **2**/$PC_{71}BM$ devices.

Taking all of the above characterization results into consideration, we see that the most profound influence on the device performance of single-atom substitution is the change in the small-molecule solubility. Despite subtle differences in the optical properties and energy levels (the typical parameters considered in the design of new small molecules or polymers for OPV devices), there are large differences in the device performance, which we propose is a result of the different BHJ morphologies. These differences in morphology (despite identical processing conditions) are likely a result of large differences in solubility between **1** and **2**. Given that **1** has a much lower solubility than **2**, we would expect a much coarser and poorly distributed morphology because the small molecules will solidify much sooner than $PC_{71}BM$. Also, the greater solubility of **2** allows for a greater range of processing parameters (i.e., casting temperature), which ultimately results in improved device performance as result of the increased morphological control.

CONCLUSIONS

In conclusion, two low-band-gap conjugated small molecules, **1** (E_g = 1.7 eV) and **2** (E_g = 1.6 eV), were synthesized, characterized, and incorporated into OPV devices. While the one-atom variation, S for Se, in these two small molecules did result in small changes with respect to electronics (i.e., band structure, band gap), the observed differences in the OPV device performance were shown to be far more dependent upon morphological differences in the resulting BHJ film when paired with $PC_{71}BM$. Overall, while the current research in heteroatom engineering is an effective and important approach toward the development of higher-efficiency organic solar cells, attention needs to be paid to seemingly mundane but critical details, such as the solubility, solid-state crystallization, and packing, and the resulting morphology within the device and not simply electronic considerations.

EXPERIMENTAL SECTION

Materials and Methods. **S1**,[27] **S5**,[27] and **S7**[49] were prepared according to reported procedures. Detailed synthetic procedures for **S2**, **S3**, and **S6** are shown in the SI. Tetrahydrofuran (THF) and toluene were purified using a pure solvent purification system prior to use. All other reagents were used as received. All reactions were carried out under an inert atmosphere using standard Schlenk techniques or in a glovebox.

^1H, ^{13}C, and ^{19}F NMR spectra were recorded on a Varian Inova-400 or VNMRS-500 spectrometer. Mass spectra were obtained on an Agilent 6220 spectrometer. Mass spectra were obtained on an Agilent 6220 spectrometer or Bruker Ultraflextreme MALDI TOF/TOF system (Bruker Daltonics, Bremen, GmbH). Elemental analyses were performed by the Analytical and Instrumentation Laboratory at the University of Alberta. UV−vis measurements were performed using Varian Cary 300 Scan and PerkinElmer Lambda 1050 spectrophotometers. TGA and DSC were carried out on PerkinElmer instrument under a nitrogen flow at a heating rate of 10 °C min^{-1}. GIXRD was performed using a Bruker D8 Discover instrument with a Cu Ka beam (40 kV, 40 mA; λ = 1.541784 Å, angle of incidence = 0.3°). Theoretical calculations were carried out at the B3LYP/6-31G(d) level using the *Gaussian 03* suite of programs.[61] AFM was performed in tapping mode on a Digital Instruments/Veeco multimode tapping atomic force microscope, and the collected data were analyzed using the open source software *Gwyddion*.

OPV Device Fabrication and Testing. OPV devices consisted of the following architecture: ITO/PEDOT:PSS/active layer/LiF/Al/Mg, where the photoactive layer consists of a BHJ formed from either **1**/$PC_{71}BM$ or **2**/$PC_{71}BM$. ITO-coated glass substrates were cleaned via sequential 10 min ultrasonication in methylene chloride, distilled water, and isopropyl alcohol, followed by a 10 min air plasma with a Harrick plasma cleaner (0.1 Torr, PDC 32G, 18 W). PEDOT:PSS (Heraeus Clevios PVP AI 4083) was filtered with a 0.2 μm cellulose acetate filter directly onto the freshly cleaned ITO substrates and spin-coated at 3000 rpm for 1 min to form a ∼30-nm-thick layer, which was annealed in air for 10 min at 120 °C. The active layer was spin-coated from a CB solution in air. The **2**/$PC_{71}BM$ blend was filtered through a 0.2 μm polytetrafluoroethylene filter before spin coating directly onto the freshly annealed PEDOT:PSS layer (on ITO). The **1**/$PC_{71}BM$ blend was spin-coated at 80 °C because of its lower solubility; 80 °C refers to the temperature of the solution, and the underlying substrate is at room temperature. The top Al (20 nm) and Mg (60 nm)

DOI: 10.1021/acsami.5b01063
ACS Appl. Mater. Interfaces 2015, 7, 8188−8199

cathodes were deposited by thermal evaporation under high-vacuum conditions (~5 × 10^{-6} Pa) at rates of ~2 and 2.5 Å s^{-1}, respectively. The device area was 0.155 ± 0.008 cm^2. After thermal deposition of the top contacts (Al and Mg), the cells were loaded into vials in a nitrogen-filed glovebox (one set of five devices per vial), sealed, and then immediately removed from the glovebox for testing. Devices were taken out of the nitrogen-filled vials one set at a time, then rapidly loaded onto the testing platform, and inserted into a custom-made environmental chamber, with an environment consisting of room temperature, dry flowing nitrogen (air exposure <5 s total during this process). The photovoltaic characteristics of the OPV devices were characterized under simulated AM 1.5G conditions (xenon source from Oriel 91191, 1000 W), equipped with a custom-made water filter and calibrated to a certified Si reference cell with a KG-5 filter (PV Measurements, PVM624). The light intensity was then subsequently measured immediately preceding any *J*−*V* curve accumulation using a thermopile (XLP12-3S-H2). *J*−*V* characteristics were recorded using a computer-controlled Keithley 2400 source meter. A minimum of three separate sets of five devices were averaged for a data point. The plus/minus values represent the standard deviation.

General Synthesis for 1 and 2. In a nitrogen-filled glovebox, a 20 mL glass tube was charged with **S5** (200 mg, 0.416 mmol) or **S6** (220 mg, 0.416 mmol), **S7** (150 mg, 0.194 mmol), $Pd(PPh_3)_4$ (20 mg, 0.017 mmol), and THF (10 mL) and sealed with a Teflon cap. The reaction mixture was heated to 150 °C for 70 min using a Biotage microwave reactor. Upon cooling to room temperature, 50 mL of CH_2Cl_2 was added to the reaction mixture and then poured into an aqueous solution of sodium diethyldithiocarbamate (1 g/100 mL) and stirred for 12 h at room temperature. Afterward, the organic layer was separated and the volatiles were reduced to ca. 10 mL, followed by precipitated with 100 mL. The dark solids were washed with MeOH (30 mL × 2) and acetone (30 mL) to obtain the pure product as a metallic purple solid. Yield: ca. 80−90%. The syntheses of the precursors for **1** and **2** are described in the SI.

Characterization for ***1****.* ^{1}H NMR (C_6D_6, 400 MHz, 60 °C): δ 8.88 (s, 2 H; Ar), 7.71 (d, *J* = 4.0 Hz, 2 H; Ar), 7.32 (d, *J* = 13.2 Hz, 2 H; Ar), 6.90 (m, 4 H; Ar), 6.42 (d, *J* = 4.0 Hz, 2 H; Ar), 4.41 (d, *J* = 5.2 Hz, 4 H; OCH_2), 2.53 (t, *J* = 8.0 Hz, 4 H; CH_2), 1.95−1.52 (m, 24 H), 1.20 (m, 16 H), 1.05 (t, *J* = 7.2 Hz, 6 H; CH_3), 0.83 (t, *J* = 7.2 Hz, 6 H; CH_3). ^{19}F NMR (C_6D_6, 376 MHz, 60 °C): δ −106.5. ^{13}C NMR (C_6D_6, 100.6 MHz, 60 °C): δ 161.1, 158.5, 153.5 (d), 149.5, 145.9, 144.7, 140.7, 136.0, 134.6, 132.9, 132.3, 130.4, 129.1, 124.7, 123.7, 123.3, 115.4, 115.5, 111.1, 75.8, 41.1, 31.4, 31.2, 30.9, 29.9, 29.5, 28.6, 24.2, 23.2, 22.3, 13.9, 13.6, 11.3. HRMS (MALDI). Calcd for $C_{66}H_{72}F_2N_4O_2S_8$ [M]: *m*/*z* 1246.3389. Found: *m*/*z* 1246.3375. Elem anal. Calcd for $C_{66}H_{72}F_2N_4O_2S_8$: C, 63.53; H, 5.82; N, 4.49; S, 20.55. Found: C, 63.58; H, 5.83; N, 4.45; S, 20.65.

Characterization for ***2****.* ^{1}H NMR (C_6D_6, 400 MHz, 60 °C): δ 8.89 (s, 2 H; Ar), 7.62 (d, *J* = 4.0 Hz, 2 H; Ar), 7.32 (d, *J* = 13.6 Hz, 2 H; Ar), 6.97 (m, 4 H; Ar), 6.45 (d, *J* = 4.0 Hz, 2 H; Ar), 4.42 (d, *J* = 5.2 Hz, 4 H; OCH_2), 2.54 (t, *J* = 8.0 Hz, 4 H; CH_2), 1.90−1.10 (m, 24 H), 0.99 (t, *J* = 7.2 Hz, 6 H; CH_3), 0.82 (t, *J* = 6.8 Hz, 6 H; CH_3). ^{19}F NMR (C_6D_6, 376 MHz, 60 °C): δ −106.2. ^{13}C NMR (C_6D_6, 100.6 MHz, 60 °C): δ 161.76, 159.21, 158.30 (d), 155.03, 145.67, 144.62, 141.14, 136.41 (d), 134.88, 133.40 (d), 132.33, 130.55 (d), 128.67, 124.72, 123.90 (d), 123.55, 123.03, 115.75 (d), 111.81 (d), 75.68, 41.06, 31.42, 31.22, 30.90, 29.98, 29.49, 28.67, 24.23, 23.27, 22.43, 14.09, 13.69, 11.43. HRMS (MALDI). Calcd for $C_{66}H_{72}F_2N_4O_2S_6Se_2$ [M]: *m*/*z* 1342.2278. Found: *m*/*z* 1342.2285. Elem anal. Calcd for $C_{66}H_{72}F_2N_4O_2S_6Se_2{\cdot}CH_3OH$: C, 58.58; H, 5.58; N, 4.08; S, 14.00. Found: C, 58.81; H, 5.60; N, 4.02; S, 13.88.

■ ASSOCIATED CONTENT

Supporting Information

Detailed synthetic procedures for **S2**, **S3** and **S6**, TGA, SEM images, UPS data, additional device characterization, supplementary AFM characterization, spectroscopic characterization of intermediates and final products (^{1}H, ^{13}C, and ^{19}F NMR), and optimized structure coordinates of **1′** and **2′**. This material is available free of charge via the Internet at http://pubs.acs.org.

■ AUTHOR INFORMATION

Corresponding Author

*E-mail: jburiak@ualberta.ca.

Author Contributions

§These authors contributed equally.

Notes

The authors declare no competing financial interest.

■ ACKNOWLEDGMENTS

Generous funding from SABIC is gratefully acknowledged. Alberta Innovates-Technology Futures of the Alberta Government, Canadian Foundation for Innovation, and Natural Sciences and Engineering Research Council of Canada are thanked for support. We are thankful for Compute Canada, having provided computational time.

■ REFERENCES

(1) Cheng, Y.-J.; Yang, S.-H.; Hsu, C.-S. Synthesis of Conjugated Polymers for Organic Solar Cell Applications. *Chem. Rev.* **2009**, *109*, 5868−5923.

(2) Beaujuge, P. M.; Fréchet, J. M. J. Molecular Design and Ordering Effects in Π-Functional Materials for Transistor and Solar Cell Applications. *J. Am. Chem. Soc.* **2011**, *133*, 20009−20029.

(3) Espinosa, N.; Hosel, M.; Jorgensen, M.; Krebs, F. C. Large Scale Deployment of Polymer Solar Cells on Land, on Sea and in the Air. *Energy Environ. Sci.* **2014**, *7*, 855−866.

(4) Brabec, C. J.; Gowrisanker, S.; Halls, J. J. M.; Laird, D.; Jia, S.; Williams, S. P. Polymer−Fullerene Bulk-Heterojunction Solar Cells. *Adv. Mater.* **2010**, *22*, 3839−3856.

(5) Li, G.; Zhu, R.; Yang, Y. Polymer Solar Cells. *Nat. Photonics* **2012**, *6*, 153−161.

(6) Bredas, J.-L.; Durrant, J. R. Organic Photovoltaics. *Acc. Chem. Res.* **2009**, *42*, 1689−1690.

(7) Dimitrov, S. D.; Durrant, J. R. Materials Design Considerations for Charge Generation in Organic Solar Cells. *Chem. Mater.* **2013**, *26*, 616−630.

(8) Mazzio, K. A.; Luscombe, C. K. The Future of Organic Photovoltaics. *Chem. Soc. Rev.* **2015**, *44*, 78−90.

(9) Dang, M. T.; Hirsch, L.; Wantz, G. P3HT:PCBM, Best Seller in Polymer Photovoltaic Research. *Adv. Mater.* **2011**, *23*, 3597−3602.

(10) He, Z.; Zhong, C.; Su, S.; Xu, M.; Wu, H.; Cao, Y. Enhanced Power-Conversion Efficiency in Polymer Solar Cells Using an Inverted Device Structure. *Nat. Photonics* **2012**, *6*, 591−595.

(11) You, J.; Dou, L.; Yoshimura, K.; Kato, T.; Ohya, K.; Moriarty, T.; Emery, K.; Chen, C.-C.; Gao, J.; Li, G.; Yang, Y. A Polymer Tandem Solar Cell with 10.6% Power Conversion Efficiency. *Nat. Commun.* **2013**, *4*, 1446.

(12) Boudreault, P.-L. T.; Najari, A.; Leclerc, M. Processable Low-Bandgap Polymers for Photovoltaic Applications. *Chem. Mater.* **2010**, *23*, 456−469.

(13) Xu, T.; Yu, L. How to Design Low Bandgap Polymers for Highly Efficient Organic Solar Cells. *Mater. Today* **2014**, *17*, 11−15.

(14) Ashraf, R. S.; Schroeder, B. C.; Bronstein, H. A.; Huang, Z.; Thomas, S.; Kline, R. J.; Brabec, C. J.; Rannou, P.; Anthopoulos, T. D.; Durrant, J. R.; McCulloch, I. The Influence of Polymer Purification on Photovoltaic Device Performance of a Series of Indacenodithiophene Donor Polymers. *Adv. Mater.* **2013**, *25*, 2029−2034.

(15) Kingsley, J. W.; Marchisio, P. P.; Yi, H.; Iraqi, A.; Kinane, C. J.; Langridge, S.; Thompson, R. L.; Cadby, A. J.; Pearson, A. J.; Lidzey, D. G.; Jones, R. A. L.; Parnell, A. J. Molecular Weight Dependent Vertical Composition Profiles of PCDTBT:$PC_{71}BM$ Blends for Organic Photovoltaics. *Sci. Rep.* **2014**, *4*, 5286.

DOI: 10.1021/acsami.5b01063
ACS Appl. Mater. Interfaces 2015, 7, 8188−8199

(16) Walker, B.; Kim, C.; Nguyen, T.-Q. Small Molecule Solution-Processed Bulk Heterojunction Solar Cells. *Chem. Mater.* **2010**, *23*, 470−482.
(17) Mishra, A.; Bäuerle, P. Small Molecule Organic Semiconductors on the Move: Promises for Future Solar Energy Technology. *Angew. Chem., Int. Ed.* **2012**, *51*, 2020−2067.
(18) Coughlin, J. E.; Henson, Z. B.; Welch, G. C.; Bazan, G. C. Design and Synthesis of Molecular Donors for Solution-Processed High-Efficiency Organic Solar Cells. *Acc. Chem. Res.* **2013**, *47*, 257−270.
(19) Chen, Y.; Wan, X.; Long, G. High Performance Photovoltaic Applications Using Solution-Processed Small Molecules. *Acc. Chem. Res.* **2013**, *46*, 2645−2655.
(20) Sun, Y.; Welch, G. C.; Leong, W. L.; Takacs, C. J.; Bazan, G. C.; Heeger, A. J. Solution-Processed Small-Molecule Solar Cells with 6.7% Efficiency. *Nat. Mater.* **2012**, *11*, 44−48.
(21) Lai, L. F.; Love, J. A.; Sharenko, A.; Coughlin, J. E.; Gupta, V.; Tretiak, S.; Nguyen, T.-Q.; Wong, W.-Y.; Bazan, G. C. Topological Considerations for the Design of Molecular Donors with Multiple Absorbing Units. *J. Am. Chem. Soc.* **2014**, *136*, 5591−5594.
(22) Zhou, J.; Zuo, Y.; Wan, X.; Long, G.; Zhang, Q.; Ni, W.; Liu, Y.; Li, Z.; He, G.; Li, C.; Kan, B.; Li, M.; Chen, Y. Solution-Processed and High-Performance Organic Solar Cells Using Small Molecules with a Benzodithiophene Unit. *J. Am. Chem. Soc.* **2013**, *135*, 8484−8487.
(23) Liu, J.; Sun, Y.; Moonsin, P.; Kuik, M.; Proctor, C. M.; Lin, J.; Hsu, B. B.; Promarak, V.; Heeger, A. J.; Nguyen, T.-Q. Tri-Diketopyrrolopyrrole Molecular Donor Materials for High-Performance Solution-Processed Bulk Heterojunction Solar Cells. *Adv. Mater.* **2013**, *25*, 5898−5903.
(24) Liu, Y.; Yang, Y.; Chen, C.-C.; Chen, Q.; Dou, L.; Hong, Z.; Li, G.; Yang, Y. Solution-Processed Small Molecules Using Different Electron Linkers for High-Performance Solar Cells. *Adv. Mater.* **2013**, *25*, 4657−4662.
(25) Bura, T.; Leclerc, N.; Fall, S.; Lévêque, P.; Heiser, T.; Retailleau, P.; Rihn, S.; Mirloup, A.; Ziessel, R. High-Performance Solution-Processed Solar Cells and Ambipolar Behavior in Organic Field-Effect Transistors with Thienyl-BODIPY Scaffoldings. *J. Am. Chem. Soc.* **2012**, *134*, 17404−17407.
(26) Roncali, J.; Leriche, P.; Blanchard, P. Molecular Materials for Organic Photovoltaics: Small Is Beautiful. *Adv. Mater.* **2014**, *26*, 3821−3838.
(27) van der Poll, T. S.; Love, J. A.; Nguyen, T.-Q.; Bazan, G. C. Non-Basic High-Performance Molecules for Solution-Processed Organic Solar Cells. *Adv. Mater.* **2012**, *24*, 3646−3649.
(28) Kyaw, A. K. K.; Wang, D. H.; Wynands, D.; Zhang, J.; Nguyen, T.-Q.; Bazan, G. C.; Heeger, A. J. Improved Light Harvesting and Improved Efficiency by Insertion of an Optical Spacer (ZnO) in Solution-Processed Small-Molecule Solar Cells. *Nano Lett.* **2013**, *13*, 3796−3801.
(29) Love, J. A.; Nagao, I.; Huang, Y.; Kuik, M.; Gupta, V.; Takacs, C. J.; Coughlin, J. E.; Qi, L.; van der Poll, T. S.; Kramer, E. J.; Heeger, A. J.; Nguyen, T.-Q.; Bazan, G. C. Silaindacenodithiophene-Based Molecular Donor: Morphological Features and Use in the Fabrication of Compositionally Tolerant, High-Efficiency Bulk Heterojunction Solar Cells. *J. Am. Chem. Soc.* **2014**, *136*, 3597−3606.
(30) Eisenmenger, N. D.; Su, G. M.; Welch, G. C.; Takacs, C. J.; Bazan, G. C.; Kramer, E. J.; Chabinyc, M. L. Effect of Bridging Atom Identity on the Morphological Behavior of Solution-Processed Small Molecule Bulk Heterojunction Photovoltaics. *Chem. Mater.* **2013**, *25*, 1688−1698.
(31) Lu, H.-I.; Lu, C.-W.; Lee, Y.-C.; Lin, H.-W.; Lin, L.-Y.; Lin, F.; Chang, J.-H.; Wu, C.-I.; Wong, K.-T. New Molecular Donors with Dithienopyrrole as the Electron-Donating Group for Efficient Small-Molecule Organic Solar Cells. *Chem. Mater.* **2014**, *26*, 4361−4367.
(32) Bai, H.; Wang, Y.; Cheng, P.; Li, Y.; Zhu, D.; Zhan, X. Acceptor−Donor−Acceptor Small Molecules Based on Indacenodithiophene for Efficient Organic Solar Cells. *ACS Appl. Mater. Interfaces* **2014**, *6*, 8426−8433.
(33) Lin, Y.; Ma, L.; Li, Y.; Liu, Y.; Zhu, D.; Zhan, X. Small-Molecule Solar Cells with Fill Factors up to 0.75 Via a Layer-by-Layer Solution Process. *Adv. Energy Mater.* **2014**, *4*, 1300626.
(34) Chen, J.; Cao, Y. Development of Novel Conjugated Donor Polymers for High-Efficiency Bulk-Heterojunction Photovoltaic Devices. *Acc. Chem. Res.* **2009**, *42*, 1709−1718.
(35) Scharber, M. C.; Koppe, M.; Gao, J.; Cordella, F.; Loi, M. A.; Denk, P.; Morana, M.; Egelhaaf, H.-J.; Forberich, K.; Dennler, G.; Gaudiana, R.; Waller, D.; Zhu, Z.; Shi, X.; Brabec, C. J. Influence of the Bridging Atom on the Performance of a Low-Bandgap Bulk Heterojunction Solar Cell. *Adv. Mater.* **2010**, *22*, 367−370.
(36) Blouin, N.; Michaud, A.; Leclerc, M. A Low-Bandgap Poly(2,7-carbazole) Derivative for Use in High-Performance Solar Cells. *Adv. Mater.* **2007**, *19*, 2295−2300.
(37) Zhou, H.; Yang, L.; Stuart, A. C.; Price, S. C.; Liu, S.; You, W. Development of Fluorinated Benzothiadiazole as a Structural Unit for a Polymer Solar Cell of 7% Efficiency. *Angew. Chem., Int. Ed.* **2011**, *50*, 2995−2998.
(38) He, X.; Baumgartner, T. Conjugated Main-Group Polymers for Optoelectronics. *RSC Adv.* **2013**, *3*, 11334−11350.
(39) Gibson, G. L.; McCormick, T. M.; Seferos, D. S. Atomistic Band Gap Engineering in Donor−Acceptor Polymers. *J. Am. Chem. Soc.* **2011**, *134*, 539−547.
(40) He, G.; Kang, L.; Torres Delgado, W.; Shynkaruk, O.; Ferguson, M. J.; McDonald, R.; Rivard, E. The Marriage of Metallacycle Transfer Chemistry with Suzuki−Miyaura Cross-Coupling to Give Main Group Element-Containing Conjugated Polymers. *J. Am. Chem. Soc.* **2013**, *135*, 5360−5363.
(41) Park, Y. S.; Wu, Q.; Nam, C.-Y.; Grubbs, R. B. Polymerization of Tellurophene Derivatives by Microwave-Assisted Palladium-Catalyzed *ipso*-Arylative Polymerization. *Angew. Chem., Int. Ed.* **2014**, *53*, 10691−10695.
(42) Lee, J.; Han, A. R.; Kim, J.; Kim, Y.; Oh, J. H.; Yang, C. Solution-Processable Ambipolar Diketopyrrolopyrrole−Selenophene Polymer with Unprecedentedly High Hole and Electron Mobilities. *J. Am. Chem. Soc.* **2012**, *134*, 20713−20721.
(43) Dou, L.; Chang, W.-H.; Gao, J.; Chen, C.-C.; You, J.; Yang, Y. A Selenium-Substituted Low-Bandgap Polymer with Versatile Photovoltaic Applications. *Adv. Mater.* **2013**, *25*, 825−831.
(44) Kronemeijer, A. J.; Gili, E.; Shahid, M.; Rivnay, J.; Salleo, A.; Heeney, M.; Sirringhaus, H. A Selenophene-Based Low-Bandgap Donor−Acceptor Polymer Leading to Fast Ambipolar Logic. *Adv. Mater.* **2012**, *24*, 1558−1565.
(45) Warnan, J.; El Labban, A.; Cabanetos, C.; Hoke, E. T.; Shukla, P. K.; Risko, C.; Brédas, J.-L.; McGehee, M. D.; Beaujuge, P. M. Ring Substituents Mediate the Morphology of PBDTTPD−PCBM Bulk-Heterojunction Solar Cells. *Chem. Mater.* **2014**, *26*, 2299−2306.
(46) Carrera, E. I.; Seferos, D. S. Semiconducting Polymers Containing Tellurium: Perspectives toward Obtaining High-Performance Materials. *Macromolecules* **2014**, *48*, 297−308.
(47) Gibson, G. L.; McCormick, T. M.; Seferos, D. S. Effect of Group-14 and Group-16 Substitution on the Photophysics of Structurally Related Donor−Acceptor Polymers. *J. Phys. Chem. C* **2013**, *117*, 16606−16615.
(48) Das, S.; Pati, P. B.; Zade, S. S. Cyclopenta[*c*]thiophene-Based D−A Conjugated Copolymers: Effect of Heteroatoms (S, Se, and N) of Benzazole Acceptors on the Properties of Polymers. *Macromolecules* **2012**, *45*, 5410−5417.
(49) Hou, J.; Park, M.-H.; Zhang, S.; Yao, Y.; Chen, L.-M.; Li, J.-H.; Yang, Y. Bandgap and Molecular Energy Level Control of Conjugated Polymer Photovoltaic Materials Based on Benzo[1,2-*b*:4,5-*b*′]-dithiophene. *Macromolecules* **2008**, *41*, 6012−6018.
(50) Hou, J.; Chen, T. L.; Zhang, S.; Chen, H.-Y.; Yang, Y. Poly[4,4-bis(2-ethylhexyl)cyclopenta[2,1-*b*;3,4-*b*′]dithiophene-2,6-diyl-*alt*-2,1,3-benzoselenadiazole-4,7-diyl], a New Low Band Gap Polymer in Polymer Solar Cells. *J. Phys. Chem. C* **2009**, *113*, 1601−1605.
(51) Yang, R.; Tian, R.; Hou, Q.; Yang, W.; Cao, Y. Synthesis and Optical and Electroluminescent Properties of Novel Conjugated

DOI: 10.1021/acsami.5b01063
ACS Appl. Mater. Interfaces 2015, 7, 8188−8199

Copolymers Derived from Fluorene and Benzoselenadiazole. *Macromolecules* **2003**, *36*, 7453−7460.
(52) Pati, P. B.; Zade, S. S. Benzoselenadiazole Containing Donor−Acceptor−Donor Small Molecules: Nonbonding Interactions, Packing Patterns, and Optoelectronic Properties. *Cryst. Growth Des.* **2014**, *14*, 1695−1700.
(53) Zou, Y.; Najari, A.; Berrouard, P.; Beaupré, S.; Réda Aïch, B.; Tao, Y.; Leclerc, M. A Thieno[3,4-*c*]pyrrole-4,6-dione-Based Copolymer for Efficient Solar Cells. *J. Am. Chem. Soc.* **2010**, *132*, 5330−5331.
(54) Piliego, C.; Holcombe, T. W.; Douglas, J. D.; Woo, C. H.; Beaujuge, P. M.; Fréchet, J. M. J. Synthetic Control of Structural Order in *N*-Alkylthieno[3,4-*c*]pyrrole-4,6-dione-Based Polymers for Efficient Solar Cells. *J. Am. Chem. Soc.* **2010**, *132*, 7595−7597.
(55) Worfolk, B. J.; Hauger, T. C.; Harris, K. D.; Rider, D. A.; Fordyce, J. A. M.; Beaupré, S.; Leclerc, M.; Buriak, J. M. Work Function Control of Interfacial Buffer Layers for Efficient and Air-Stable Inverted Low-Bandgap Organic Photovoltaics. *Adv. Energy Mater.* **2012**, *2*, 361−368.
(56) Hollinger, J.; Gao, D.; Seferos, D. S. Selenophene Electronics. *Isr. J. Chem.* **2014**, *54*, 440−453.
(57) Heeney, M.; Zhang, W.; Crouch, D. J.; Chabinyc, M. L.; Gordeyev, S.; Hamilton, R.; Higgins, S. J.; McCulloch, I.; Skabara, P. J.; Sparrowe, D.; Tierney, S. Regioregular Poly(3-hexyl)selenophene: A Low Band Gap Organic Hole Transporting Polymer. *Chem. Commun.* **2007**, 5061−5063.
(58) Hollinger, J.; Jahnke, A. A.; Coombs, N.; Seferos, D. S. Controlling Phase Separation and Optical Properties in Conjugated Polymers through Selenophene−Thiophene Copolymerization. *J. Am. Chem. Soc.* **2010**, *132*, 8546−8547.
(59) Würthner, F.; Kaiser, T. E.; Saha-Möller, C. R. J-Aggregates: From Serendipitous Discovery to Supramolecular Engineering of Functional Dye Materials. *Angew. Chem., Int. Ed.* **2011**, *50*, 3376−3410.
(60) Spano, F. C.; Silva, C. H- and J-Aggregate Behavior in Polymeric Semiconductors. *Annu. Rev. Phys. Chem.* **2014**, *65*, 477−500.
(61) Frisch, M. J.; Trucks, G. W.; Schlegel, H. B.; Scuseria, G. E.; Robb, M. A.; Cheeseman, J. R.; Scalmani, G.; Barone, V.; Mennucci, B.; Petersson, G. A.; Nakatsuji, H.; Caricato, M.; Li, X.; Hratchian, H. P.; Izmaylov, A. F.; Bloino, J.; Zheng, G.; Sonnenberg, J. L.; Hada, M.; Ehara, M.; Toyota, K.; Fukuda, R.; Hasegawa, J.; Ishida, M.; Nakajima, T.; Honda, Y.; Kitao, O.; Nakai, H.; Vreven, T.; Montgomery, J. A., Jr.; Peralta, J. E.; Ogliaro, F.; Bearpark, M.; Heyd, J. J.; Brothers, E.; Kudin, K. N.; Staroverov, V. N.; Kobayashi, R.; Normand, J.; Raghavachari, K.; Rendell, A.; Burant, J. C.; Iyengar, S. S.; Tomasi, J.; Cossi, M.; Rega, N.; Millam, J. M.; Klene, M.; Knox, J. E.; Cross, J. B.; Bakken, V.; Adamo, C.; Jaramillo, J.; Gomperts, R.; Stratmann, R. E.; Yazyev, O.; Austin, A. J.; Cammi, R.; Pomelli, C.; Ochterski, J. W.; Martin, R. L.; Morokuma, K.; Zakrzewski, V. G.; Voth, G. A.; Salvador, P.; Dannenberg, J. J.; Dapprich, S.; Daniels, A. D.; Farkas, Ö.; Foresman, J. B.; Ortiz, J. V.; Cioslowski, J.; Fox, D. J. *Gaussian 09*, revision A.02; Gaussian, Inc.: Wallingford, CT, 2009.
(62) Agostinelli, T.; Lilliu, S.; Labram, J. G.; Campoy-Quiles, M.; Hampton, M.; Pires, E.; Rawle, J.; Bikondoa, O.; Bradley, D. D. C.; Anthopoulos, T. D.; Nelson, J.; Macdonald, J. E. Real-Time Investigation of Crystallization and Phase-Segregation Dynamics in P3HT:PCBM Solar Cells during Thermal Annealing. *Adv. Funct. Mater.* **2011**, *21*, 1701−1708.
(63) Huang, W. Y.; Huang, P. T.; Han, Y. K.; Lee, C. C.; Hsieh, T. L.; Chang, M. Y. Aggregation and Gelation Effects on the Performance of Poly(3-hexylthiophene)/Fullerene Solar Cells. *Macromolecules* **2008**, *41*, 7485−7489.
(64) Zhang, Q.; Kan, B.; Liu, F.; Long, G.; Wan, X.; Chen, X.; Zuo, Y.; Ni, W.; Zhang, H.; Li, M.; Hu, Z.; Huang, F.; Cao, Y.; Liang, Z.; Zhang, M.; Russell, T. P.; Chen, Y. Small-Molecule Solar Cells with Efficiency over 9%. *Nat. Photonics* **2015**, *9*, 35−41.
(65) Chabinyc, M. L.; Toney, M. F.; Kline, R. J.; McCulloch, I.; Heeney, M. X-Ray Scattering Study of Thin Films of Poly(2,5-bis(3-alkylthiophen-2-yl)thieno[3,2-*b*]thiophene. *J. Am. Chem. Soc.* **2007**, *129*, 3226−3237.
(66) McCulloch, I.; Heeney, M.; Bailey, C.; Genevicius, K.; MacDonald, I.; Shkunov, M.; Sparrowe, D.; Tierney, S.; Wagner, R.; Zhang, W.; Chabinyc, M. L.; Kline, R. J.; McGehee, M. D.; Toney, M. F. Liquid-Crystalline Semiconducting Polymers with High Charge-Carrier Mobility. *Nat. Mater.* **2006**, *5*, 328−333.
(67) Kline, R. J.; DeLongchamp, D. M.; Fischer, D. A.; Lin, E. K.; Richter, L. J.; Chabinyc, M. L.; Toney, M. F.; Heeney, M.; McCulloch, I. Critical Role of Side-Chain Attachment Density on the Order and Device Performance of Polythiophenes. *Macromolecules* **2007**, *40*, 7960−7965.
(68) Dhar, P.; Khlyabich, P. P.; Burkhart, B.; Roberts, S. T.; Malyk, S.; Thompson, B. C.; Benderskii, A. V. Annealing-Induced Changes in the Molecular Orientation of Poly-3-hexylthiophene at Buried Interfaces. *J. Phys. Chem. C* **2013**, *117*, 15213−15220.
(69) Verploegen, E.; Mondal, R.; Bettinger, C. J.; Sok, S.; Toney, M. F.; Bao, Z. Effects of Thermal Annealing upon the Morphology of Polymer−Fullerene Blends. *Adv. Funct. Mater.* **2010**, *20*, 3519−3529.
(70) Rivnay, J.; Mannsfeld, S. C. B.; Miller, C. E.; Salleo, A.; Toney, M. F. Quantitative Determination of Organic Semiconductor Microstructure from the Molecular to Device Scale. *Chem. Rev.* **2012**, *112*, 5488−5519.

DOI: 10.1021/acsami.5b01063
ACS Appl. Mater. Interfaces 2015, 7, 8188−8199